Journal of Applied Geophysics 99 (2013) 114–124

Contents lists available at ScienceDirect

Journal of Applied Geophysics

journal homepage: www.elsevier.com/locate/jappgeo

Improvements in crosshole GPR full-waveform inversion and application on data measured at the Boise Hydrogeophysics Research Site

X. Yang [a], A. Klotzsche [a], G. Meles [b,1], H. Vereecken [a], J. van der Kruk [a,*]

[a] Agrosphere, IBG-3, Forschungszentrum Jülich, Jülich, 52425, Germany
[b] School of GeoSciences, The University of Edinburgh, Edinburgh EH1 2QL, United Kingdom

ARTICLE INFO

Article history:
Received 17 February 2013
Accepted 12 August 2013
Available online 27 August 2013

Keywords:
GPR
Full-waveform inversion
Normalized gradient
Logging data
Boise Research Site

ABSTRACT

Crosshole ground penetrating radar (GPR) tomography has been widely used and has the potential to improve the obtained subsurface models due to its high spatial resolution compared to other methods. Recent advances in full-waveform inversion of crosshole GPR data show that higher resolution images can be obtained compared to conventional ray-based GPR inversion because it can exploit all information present in the observed data. Since the first application of full-waveform inversion on synthetic and experimental GPR data, the algorithm has been significantly improved by extending the scalar to a vectorial approach, and changing the stepped permittivity and conductivity update into a simultaneous update. Here, we introduce new normalized gradients that do not depend on the number of sources and receivers which enable a comparison of the gradients and step lengths for different crosshole survey layouts. An experimental data set acquired at the Boise Hydrogeophysics Research Site is inverted using different source–receiver setups and the obtained permittivity and conductivity images, remaining gradients and final misfits are compared for the different versions of the full-waveform inversion. Moreover, different versions of the full-waveform inversion are applied to obtain an overview of all improvements. Most improvements result in a reducing final misfit between the measured and synthetic data and a reducing remaining gradient at the final iteration. Regions with relatively high remaining gradient amplitudes indicate less reliable inversion results. Comparison of the final full-waveform inversion results with Neutron–Neutron porosity log data and capacitive resistivity log data show considerably higher spatial frequencies for the logging data compared to the full-waveform inversion results. To enable a better comparison, we estimated a simple wavenumber filter and the full-waveform inversion results show an improved fit with the logging data. This work shows the potential of full-waveform inversion as an advanced method that can provide high resolution images to improve hydrological models.

1. Introduction

Crosshole ground penetrating radar (GPR) tomography can provide a high resolution profile of the shallow subsurface electrical properties (dielectric permittivity ε and electrical conductivity σ) between two boreholes (Holliger et al., 2001; Irving and Knight, 2005; Tronicke et al., 2002). For crosshole GPR surveys, tomographic inversions are generally based on geometrical ray theory (Dafflon and Barrash, 2012; Dafflon et al., 2011; Irving et al., 2007; Maurer and Musil, 2004). It provides electromagnetic velocity and attenuation images of the probed regions by first-arrival times and maximum first-cycle amplitude inversions. Conventional ray tomography can suffer from critical shortcomings associated with the limitation of the high-frequency approximation, the limited angular coverage of the target, and the limited information present in the observed signal that is employed in the inversion process. Furthermore, ray-based inversion usually only resolves features larger than the dominant signal wavelength (resolution scales approximately with the diameter of the first Fresnel zone) and it cannot provide reliable information on certain important types of low-velocity (high-permittivity) structures (Williamson and Worthington, 1993).

The resolution of the images can be significantly improved by using a full-waveform inversion (FWI) that considers the entire waveform or significant parts thereof (Ernst et al., 2007a). The FWI has been first proposed in exploration seismology and has been developed for both acoustic and elastic waves generated and recorded at the surface or borehole. The FWI provides sub-wavelength resolution and reliable information on a broad range of structures, including those distinguished by low velocities. To determine an update of the medium properties, the full-waveform modeling is performed at each iteration by using finite-difference or finite-element approaches that can be performed in either the time- or frequency domain (Pratt, 1990, 1999; Tarantola, 1984, 1986; Virieux and Operto, 2009; Zhou and Greenhalgh, 2003). One of the first FWIs of crosshole GPR approach was applied to synthetic

* Corresponding author. Tel.: +49 2461 614077.
E-mail address: j.van.der.kruk@fz-juelich.de (J. van der Kruk).
[1] Formerly at ETH Zürichquery.

0926-9851/$ – see front matter © 2013 Elsevier B.V. All rights reserved.
http://dx.doi.org/10.1016/j.jappgeo.2013.08.007

(Ernst et al., 2007a), and two experimental data sets (Ernst et al., 2007b); one obtained in the Grimsel rock laboratory and one obtained at the Boise Hydrogeophysics Research Site (BHRS) near Boise, Idaho, USA. Since these first applications of FWI for crosshole GPR data, the FWI has been improved by including the vector character of the electrical field and the simultaneous inversion of permittivity and conductivity (Meles et al., 2010). The improved FWI approach also was optimized and applied to an experimental data set near the River Thur in Switzerland (Klotzsche et al., 2010). The full-waveform inversion was able to reconstruct a low-velocity waveguide layer, which was caused by an increase in porosity and indicates a zone of preferential flow within the aquifer (Klotzsche et al., 2012). Compared to traditional hydrological measurements such as borehole logging and petrophysical analysis, crosshole GPR tomography provides field-scale information of the shallow subsurface. This information can improve soil water content estimation and flow change. In this respect, crosshole GPR tomography has been widely used in hydrology and showed its potential for aquifer characterization (Binley et al., 2001, 2002; Deiana et al., 2007; Hubbard et al., 1997; Looms et al., 2008; Slater et al., 1997; Winship et al., 2006). The permittivity values can be converted to effective porosity by empirical formulas such as Topp et al. (1980) and Linde et al. (2006) and hydraulic conductivity by using geostatistics and Kozeny–Carman relation (Gloaguen et al., 2001).

In the following, an overview is given of all developments by showing the improvements of the FWI to the experimental data set acquired at the BHRS. Moreover, four times as many receivers are used to investigate the improvements. Because the misfit and gradients initially were depending on the number of sources and receivers, we first introduce a normalized misfit and gradient that is independent on the number of source and receivers. After introducing the BHRS and the crosshole GPR setup, the inversion results and remaining gradients are compared between the ray-based and different version of the FWI. Finally, we evaluate the FWI results with Neutron–Neutron porosity and capacitive resistivity logging data. Due to the different spatial resolutions, a wavenumber filter is introduced that enables a better comparison.

2. Full-waveform inversion methodology

In the earlier years of the 1980, it was a challenge to invert experimental data sets measured with a large number of sources and receivers, due to the limited computing resources available. Due to the recent developments of parallel programming tools on massive parallel computer structures, considerable effort has been dedicated to develop techniques that allow solving problems involving large numbers of parameters. The FWI minimizes the full-waveform differences between the synthetic GPR data and the observed GPR data at the receiver positions for all source–receiver pairs of the GPR survey by updating the spatial distributions of the medium properties ε and σ. The misfit between the recorded and modeled data is described by the squared misfit norm $S(\varepsilon,\sigma)$:

$$S(\varepsilon,\sigma)=\frac{1}{2}\sum_{s}\sum_{r}\sum_{\tau}\left[E^{s}_{\mathrm{syn}}(\varepsilon,\sigma)-E^{s}_{\mathrm{obs}}\right]^{T}_{r,\tau}\cdot\left[E^{s}_{\mathrm{syn}}(\varepsilon,\sigma)-E^{s}_{\mathrm{obs}}\right]_{r,\tau}, \qquad (1)$$

where $E^{s}_{\mathrm{syn}}(\varepsilon,\sigma)$ and E^{s}_{obs} are the synthetic and observed data, respectively, and T denotes the adjoint operator (transpose conjugate). Note that we use here Meles et al. (2010) formalism where $E^{s}_{\mathrm{syn}}(\varepsilon,\sigma)$ and E^{s}_{obs} contain the data for all sources, receivers and observation times, such that the sum over sources s, receivers r and observation time τ in Eq. (1) returns the overall misfit to be minimized. Since the full-waveform is present within the observation time we need an accurate forward model that solves the full-waveform results of Maxwell's equations for all source–receiver combinations. Here, the FWI of crosshole GPR data is based on a 2D finite-difference time-domain (FDTD) solutions of Maxwell's equations. The medium properties ε and σ are updated using the following recipe:

1) Select initial models $\varepsilon=\varepsilon_{\mathrm{ini}}$ and $\sigma=\sigma_{\mathrm{ini}}$ (usually obtained by ray-based tomography results).
2) Compute synthetic wave fields at the receiver positions using the initial models.
3) Compute the residual wave field by subtracting the synthetic from the measured data.
4) Compute the gradient directions ∇S_{ε} and ∇S_{σ} by a cross-correlation of the synthetic wave field with the back-propagated residual wave field. Here, the cross-correlation can be scalar by only including the vertical electric wave fields, or vectorial by including the vertical and horizontal electric wave fields.
5) Compute the update directions d_{ε} and d_{σ} with the conjugate gradient (CG) method using the gradient directions ∇S_{ε} and ∇S_{σ}.
6) Compute the step lengths ζ_{ε} and ζ_{σ} using a linear step length calculation and carefully chosen perturbation factors that cannot be too large to make sure the perturbed model still lies in the linearity range and inversion overshooting is avoided, and not too small to avoid truncation (round-off) errors when dealing with small numbers (Meles et al., 2010).
7) Update the model parameters ε and σ using

$$\begin{aligned}\varepsilon^{(k+1)}&=\varepsilon^{(k)}-\zeta^{(k)}_{\varepsilon}d^{(k)}_{\varepsilon}\\ \sigma^{(k+1)}&=\sigma^{(k)}-\zeta^{(k)}_{\sigma}d^{(k)}_{\sigma},\end{aligned} \qquad (2)$$

   where k is the iteration number. Here, the approach can be the stepped or cascaded by alternately updating one parameter for certain number of iterations while keeping the other one fixed, or simultaneous by updating both parameters in one iteration.
8) Repeat steps 2 through 7 until convergence has been achieved. Usually, when the remaining residuals are less than 1%, this indicates that the inversion is converged and returns credible results.

The gradients of the misfit function with respect to permittivity and conductivity ∇S_{ε} and ∇S_{σ} are obtained by cross-correlating the incident wave field emitted from the source with the residual wave fields that are back-propagating from the receiver at all medium locations in time domain for all source and receiver combinations as follows (see Eq. (23) in Meles et al., 2010):

$$\begin{bmatrix}\nabla S_{\varepsilon}\left(x'\right)\\ \nabla S_{\sigma}\left(x'\right)\end{bmatrix}=\sum_{s}\sum_{r}\sum_{\tau}\begin{matrix}\left(\partial_t E^{s}\right)^{T}\widehat{G}^{T}\left[\Delta E^{s}\right]_{r,\tau}\\ \left(E^{s}\right)^{T}\widehat{G}^{T}\left[\Delta E^{s}\right]_{r,\tau}\end{matrix}, \qquad (3)$$

where ΔE^{s} is the residual wave field at the receiver positions and $\widehat{G}^{T}$ is the back-propagation operator. Note that the ε and σ gradients only differ for a time derivative.

Because of vertical dipole-type transmitter antennas being used in crosshole GPR, the first version of FWI (Ernst et al., 2007b; Belina et al., 2012a, b) used only the E_z component of the electric field for the calculation of the gradient and ignored the E_x component. Therefore, we call it in the following scalar FWI. However, for large vertical distances between the source and receiver positions, the E_x components can significantly contribute in the gradient calculation and should therefore be included to honor the vectorial character of the electromagnetic waves. Accordingly, we refer to this version as vector FWI (Meles et al., 2010), which can also be used to invert borehole to surface data or four-sided inversions (Meles et al., 2011).

The first FWI version initially used a stepped or cascaded approach where the permittivities were updated for a certain number of iterations while keeping the conductivities fixed and then analogously the conductivities were inverting while keeping the permittivities fixed (Ernst et al., 2007a). However, Eq. (4) indicates that at each iteration both the permittivity and conductivity gradients can be calculated. To obey the simultaneous nature of the electromagnetic wave propagation, a new simultaneous version FWI has been proposed that simultaneously updates the permittivities and conductivities at each iteration (Meles

et al., 2010). Although the new simultaneous FWI version needs two more FDTD calculations for each single iteration compared to the stepped version, in total it needs less FDTD calculations, due to the improved convergence. In addition, no arbitrary number of permittivity iterations needs to be specified before conductivity iterations are executed and vice versa, which simplifies the inversion parameterization. Fig. 1 gives an overview of the different FWI versions.

Applying the gradient equations as given in Eq. (4) for different numbers of sources and receivers in synthetic studies, we observed that using two times as many sources or receivers the gradient amplitudes are also twice as large resulting in the calculated step lengths being approximately twice as small. Note that also different perturbation factors are needed to correctly compare inversion results that use different numbers of sources and receivers. Moreover, the cost function was also roughly twice as large. To remove the dependency of the cost function, gradient, step length and perturbation factor on the used number of sources and receivers, we introduce here a normalized cost function by dividing Eq. (1) with the number of sources times the number of receivers:

$$\bar{S}(\varepsilon,\sigma)=\frac{S(\varepsilon,\sigma)}{N_s N_r}. \tag{4}$$

This results in normalized permittivity and conductivity gradients:

$$\nabla\bar{S}_\varepsilon\left(x'\right)=\frac{\nabla S_\varepsilon\left(x'\right)}{N_s N_r}, \tag{5a}$$

$$\nabla\bar{S}_\sigma\left(x'\right)=\frac{\nabla S_\sigma\left(x'\right)}{N_s N_r}. \tag{5b}$$

In the following, we will analyze these normalized gradients when using different numbers of sources and receivers.

3. Boise Hydrogeophysical Research Site and crosshole GPR survey layout

The BHRS is an experimental well field located on a gravel bar adjacent to the Boise River about 15 km from downtown Boise, Idaho, USA. At the site, geophysical and hydrologic methods were used to characterize the distribution of hydrogeological properties in heterogeneous alluvial aquifers (Barrash and Clemo, 2002; Barrash and Reboulet, 2004; Barrash et al., 1999; Mwenifumbo et al., 2009). The aquifer consists of an approximately 20 m thick gravel–sand aquifer, underlying by a red clay formation. The experimental well field consists of 13 wells that are present within the red box in Fig. 2a (Bradford et al., 2009). Within the aquifer three main units (pebble and cobble dominated) have been identified with average porosities of approximately 21%, 26%, and 23%. This zonation is largely based on the interpretation of crosshole GPR

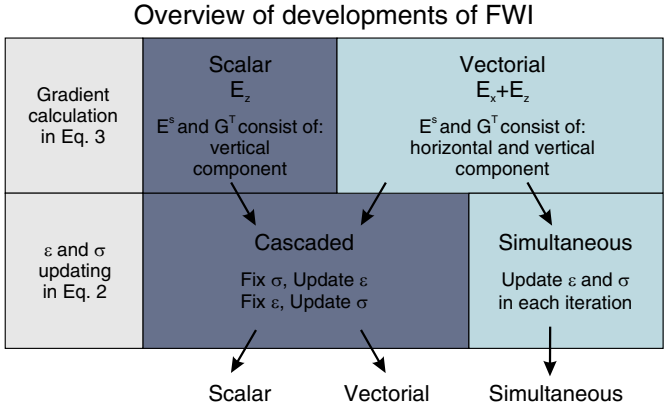

Fig. 1. Overview of main FWI developments; 1) from scalar approach which only used vertical component to vector approach which consist of vertical and horizontal component; 2) from stepped (cascaded) ε and σ update to simultaneous ε and σ update. Below the used nomenclature in the rest of the manuscript is indicated.

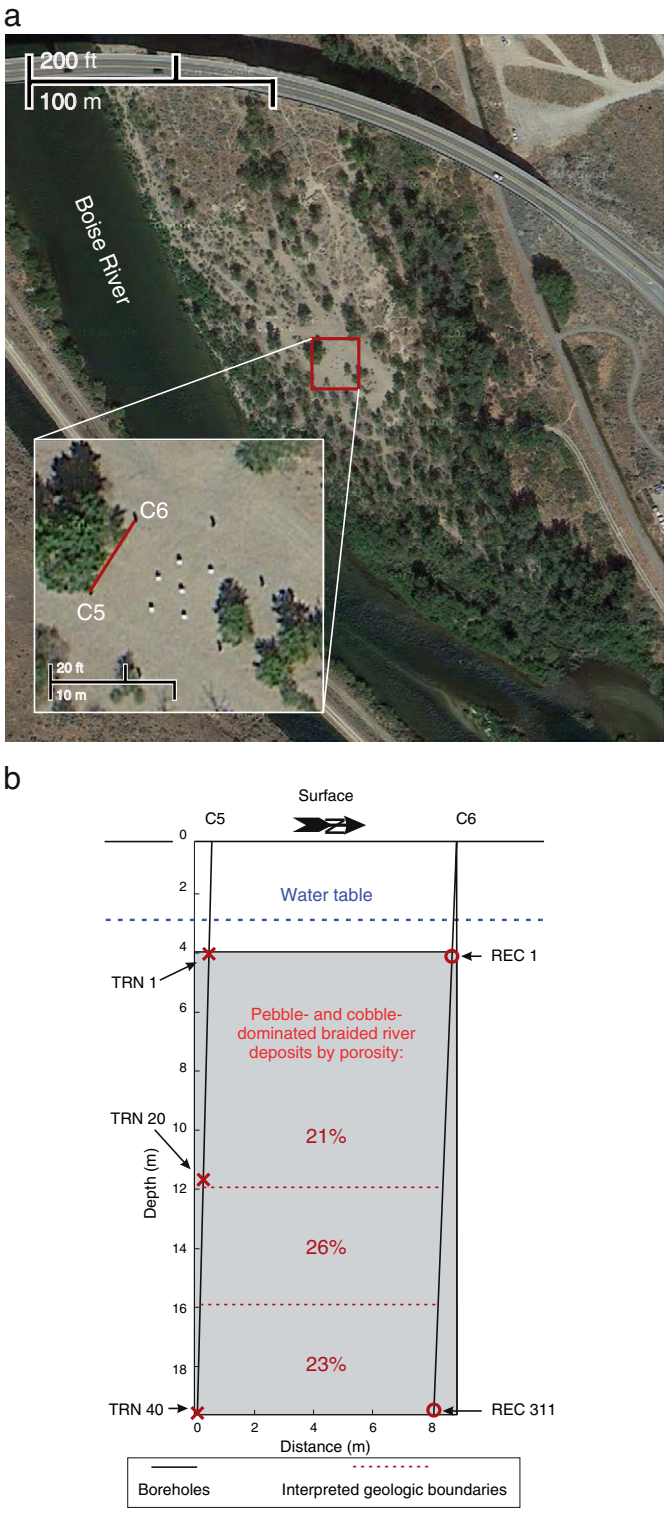

Fig. 2. (a) Location of BHRS close to the Boise River. The red line between C5 and C6 in the inset indicates the crosshole GPR profile. (b) A simplified acquisition setup of the experimental data set acquired at the BHRS. Transmitter and receiver locations are indicated by TRN with crosses and REC with circles, respectively. The unit boundaries (dashed red lines) were determined based on borehole porosity logs.
(Adapted from Ernst et al., 2007b).

data by Tronicke et al. (2004). A high quality crosshole GPR dataset was acquired in two near-vertical boreholes C5 and C6 (see Fig. 2a red line in red box) with a depth range of 20 m. The distance between the boreholes is approximately 8.5 m and the diameter of the borehole casing is 0.1 m. During the measurements, the water table was at a depth of ~3 m. The GPR data were collected using a MALÅ RAMAC Ground Vision GPR system with antennas having a nominal center frequency in air of 250 MHz (Dafflon et al., 2011). The dominant frequency for the observed data is ~80 MHz due to the borehole fluid and surrounding water-saturated sediments (Tronicke et al., 2004) and yielded a dominant wavelength of ~1 m in the low-velocity sediments. For each of the 40 transmitters with a vertical spacing of 0.4 m, the electric field was measured at 311 receiver depths with a vertical spacing of 0.05 m.

4. Results

4.1. Preprocessing

The ray-based inversion results obtained by the travel time and first-cycle amplitude inversion provide low resolution permittivity and conductivity images which are shown in Fig. 3a and b, respectively. Due to memory constraints, initial ray-based and full-waveform inversion only used 77 receiver locations with a spatial sampling of 0.4 m (Ernst et al., 2007a). Here, we also inverted the data using all 311 receiver depths.

To invert experimental data with our full-waveform inversion algorithm that uses a 2D forward modeling of Maxwell's equations, first a 3D to 2D conversion is carried out to compensate for the different geometrical spreading in 3D and 2D and the different source dimensions (Ernst et al., 2007b; Klotzsche et al., 2010). Moreover, a source wavelet needs to be estimated using a deconvolution approach (Ernst et al., 2007b; Klotzsche et al., 2010) that uses the ray-based inversion results as starting model. The source wavelet estimation using 311 receivers returned a very similar wavelet as using 77 receivers. In the following, we used the source wavelet determined using 77 receivers for consistency. Note that using the source wavelet estimated using 311 receivers returned very similar inversion results and slightly reduces the misfit compared to using the source wavelet estimated using 77 receivers.

4.2. Comparison of inversion results

All FWI versions as indicated in Fig. 1 have been applied to the crosshole GPR data acquired from boreholes C5 and C6. During the inversion the root mean square (RMS) error between the observed and

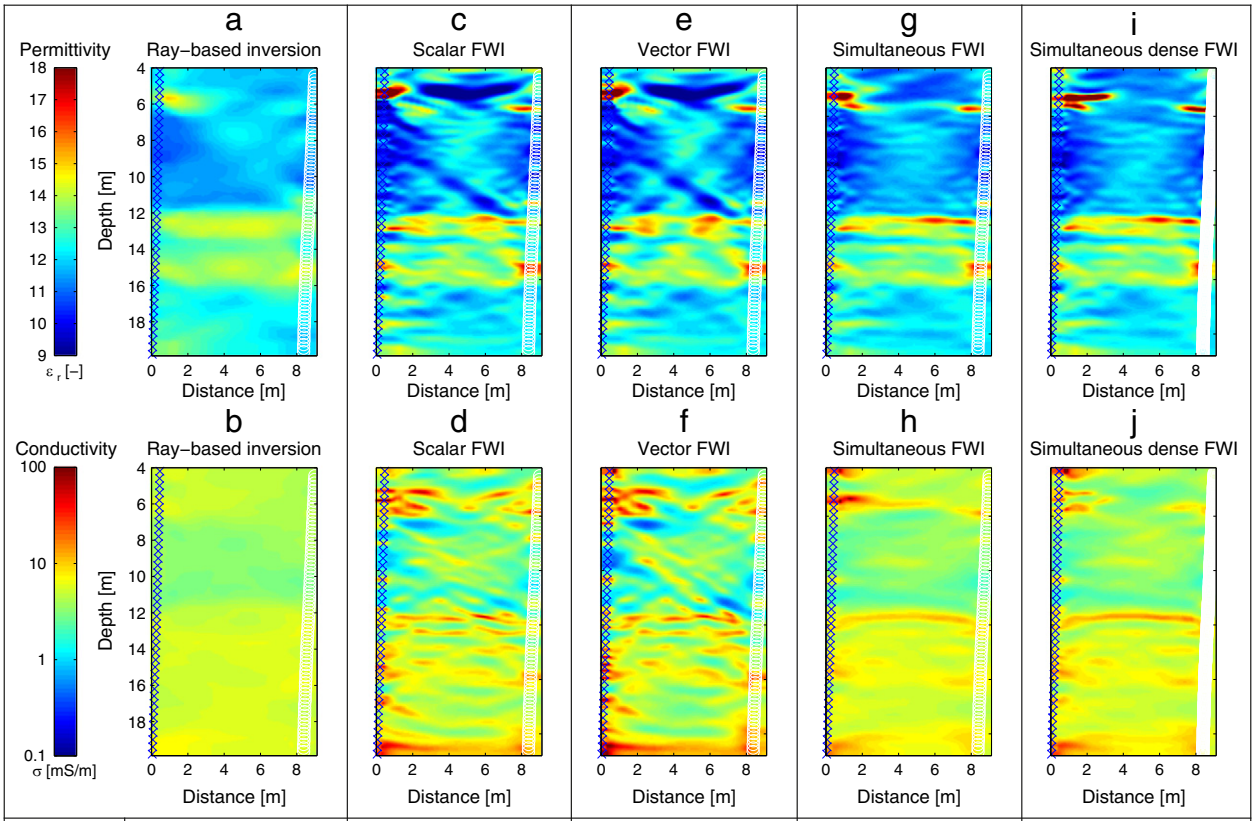

	a	c	e	g	i
Number of receivers	77	77	77	77	311
Inversion mode	-	stepped	stepped	simultaneous	simultaneous
Calculation time	~15 min	69 min	69 min	86 min	86 min
Forward models	-	180	180	120	120
RMS	3.472e-6	2.443e-6	2.398e-6	1.933e-6	1.720e-6

Fig. 3. Ray-based (a) ε and (b) σ tomography results. (c) and (d) scalar, (e) and (f) vector, (g) and (h) simultaneous, and (i) and (j) simultaneous dense ε and σ FWI inversion results, respectively. Transmitter and receivers are indicated by crosses and circles, respectively. The number of receivers, the inversion mode, calculation time, forward model number and RMS values for each method are indicated below the figures. Note the logarithmical scale of the conductivity images.

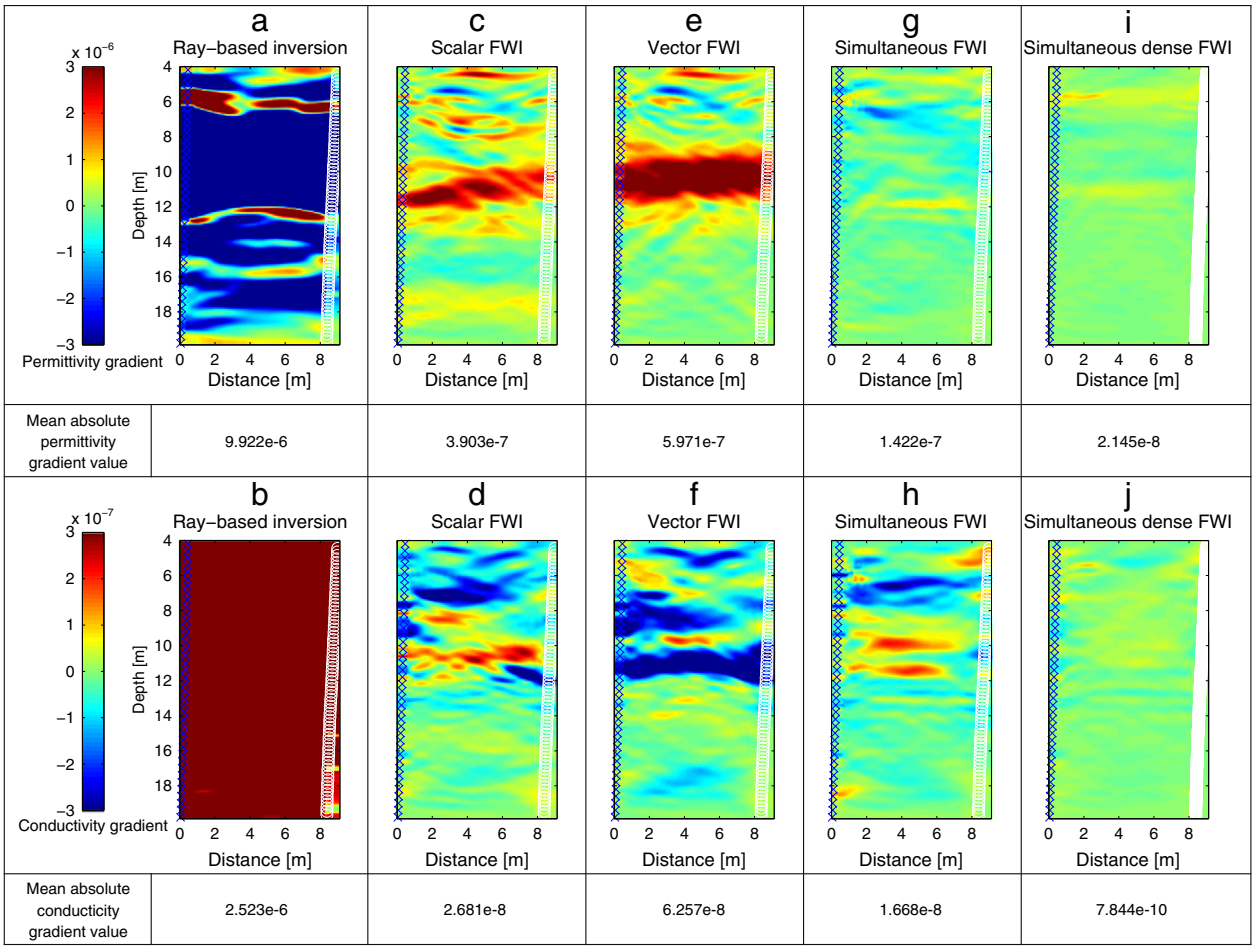

Fig. 4. Remaining gradients for the ray-based (a) ε and (b) σ tomography, respectively. Remaining gradients obtained by (c) and (d) scalar, (e) and (f) vector, (g) and (h) simultaneous, and (i) and (j) simultaneous dense ε and σ FWI results, respectively, at the last iteration. The mean absolute remaining gradient value for all the results is indicated below the figures. Note that, (a) and (b) show the gradient for the ε and σ, respectively, after one iteration of the FWI to illustrate the misfit between the ray-based inversion result and the observed data.

synthetic data over all time samples is minimized using 30 iterations. The results of the cumulative improvements of FWI are shown in Fig. 3c, j. For the FWI results in Fig. 3c, h the number of receiver positions used in the inversion is 77, whereas for Fig. 3i, j the number of receiver positions used in the inversion is 311. Throughout the rest of this paper, we use simultaneous dense FWI to indicate the simultaneous FWI using 311 receiver locations. Compared to the ray-based inversion, a higher resolution of the shallow subsurface is obtained in Fig. 3c, d by applying the scalar FWI version using the stepped approach that inverts for the permittivity while keeping the conductivities fixed and vice versa. A prominent dipping feature in the results of permittivity and conductivity between 9 m and 12 m depth is visible. The table below the figures shows the obtained RMS value between the observed and synthetic data for the final iteration number, which decreased significantly compared to the ray-based inversion. Note that the ray-based inversion results are used as starting model for the FWI. The vector FWI (Fig. 3e, f) that considers the vectorial nature of the electric fields returns similar imaging results and a slightly smaller RMS value was obtained (see the table below the figures). Next, a simultaneous FWI version of the permittivity and conductivity values is used where the step lengths and updates for these two parameters are calculated for each iteration (Meles et al., 2010). Although this process requires an additional forward model calculation for every iteration, the simultaneous nature of the process results in a reduction in the total number of forward calculations needed (Fig. 3g, h and table below). Here, the prominent dipping feature is nearly absent and the obtained RMS value is again reduced with more than 20%, which indicates that the dipping feature is a numerical artifact. Running the simultaneous dense FWI, the images show small differences from the simultaneous FWI version results using 77 receiver positions (Fig. 3i, j). However, the obtained RMS value reduced distinctly, which indicates that the current results represent well reality. Due to the sparse source sampling of 0.4 min the left borehole, and the higher spatial sampling of the receivers of 0.05 or 0.2 m most changes can be observed close to the left borehole. An optimized source–receiver setup is discussed by Klotzsche et al. (2010), and evaluated by Oberröhrmann et al. (2013). The calculation time of the ray-based tomography results is run on a single CPU PC, whereas the calculation times for all FWI results are run on a supercomputer JUROPA by parallel calculation with 41 CPUs.

4.3. Remaining gradient comparison

To investigate the reliability of the inversion results for all series of FWI, we show all remaining permittivity and conductivity gradients at the last iteration, 30, in Fig. 4a and b, respectively, using the same color scale. The mean of the absolute normalized gradient values (see Eqs. (4)–(5a), (5b)) is listed below the figures. Since the ray-based are used as start models for the FWI these gradients are calculated and used in the first iteration of the FWI. The remaining gradients for all FWI approaches are shown in Fig. 4c, j. The remaining gradients for the scalar and vector FWI version using a stepped approach shown in Fig. 4c, d, e, f show still relatively large amplitudes between 4 and 12 m. Note that in this region also the artificial dipping feature was detected. The remaining gradients for the vector FWI version are slightly

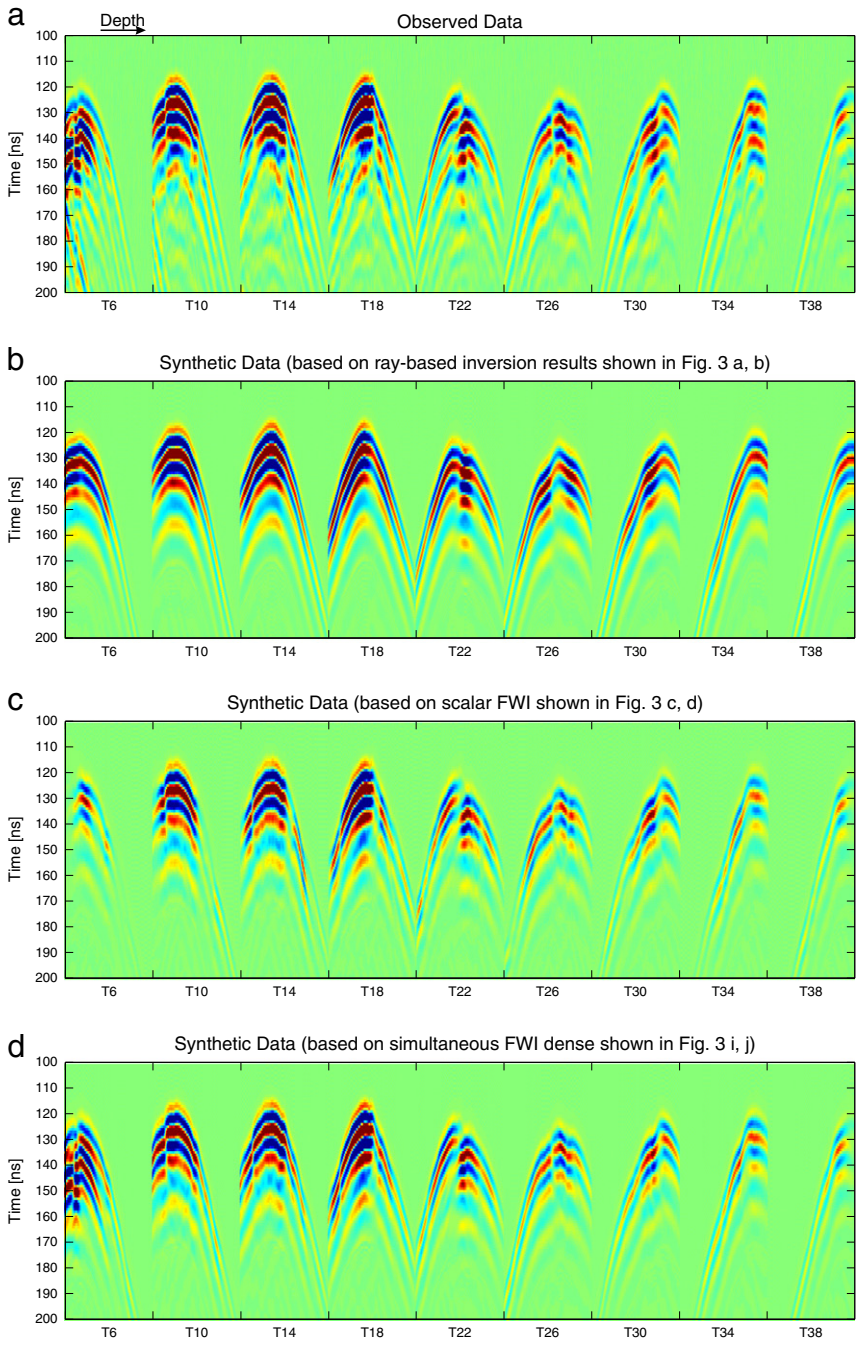

Fig. 5. Shot gathers for nine representative transmitters and forty receivers for (a) measured GPR data, synthetic data modeled using (b) ray-based tomography results shown in Fig. 3(a) and (b), (c) scalar FWI results shown in Fig. 3(c) and (d), and (d) simultaneous dense FWI results shown in Fig. 3(i) and (j), respectively. Note that no scaling is applied and only true amplitudes are shown. Note that only 9 transmitters were chosen with equal intervals from the 40 transmitters.

larger than the scalar FWI version, which is probably caused by using the two components of the vector electric fields to calculate the gradients and more data information and more energy is contributing to the gradient calculation. Smaller and more homogeneous gradients are obtained by the simultaneous FWI version (Fig. 4g, h). For the permittivity gradient, the fluctuations are strongly reduced, but for the remaining conductivity gradient, we can still observe some amplitude fluctuations. When using the simultaneous dense FWI, the absolute mean values of the remaining permittivity and conductivity gradients are significantly reduced and relatively homogeneous gradients are obtained (Fig. 4i, j). Note that the permittivity and conductivity images show only small differences compared to the simultaneous FWI results using 77 receiver positions (see Fig. 3), which indicates that the current results are stable. Summarizing, we see that almost every improvement of the FWI approach results in a decreasing absolute mean value of the remaining gradient indicated below Fig. 4. Moreover, the obtained results indicate that remaining gradients indicate regions where the inversion results are less reliable.

4.4. Observed and synthetic radar data comparison

To analyze the obtained results in more detail, we compared the measured electric field at all receiver positions (radargrams) for nine transmitters T6, T10, T14, T18, T22, T26, T30, T34 and T38 shown in Fig. 5a with the synthetically calculated electric field for the final inversion results of ray-based tomography (Fig. 5b), the scalar FWI (Fig. 5c)

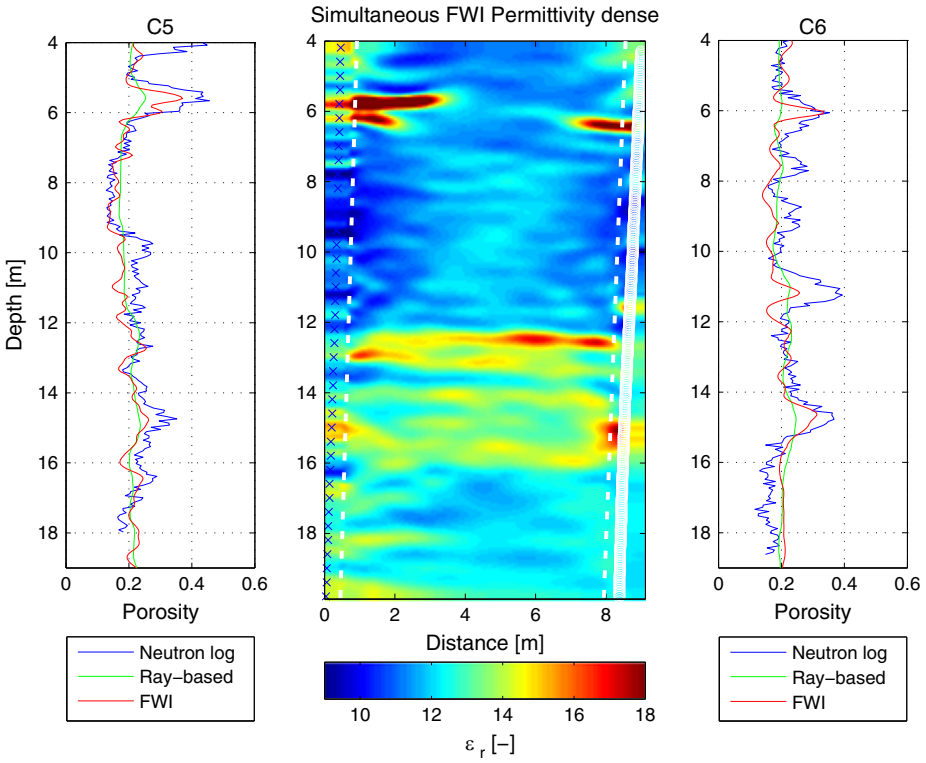

Fig. 6. Simultaneous dense permittivity FWI results at the last iteration number. Permittivity values indicated by the dashed white lines close to the C5 and C6 boreholes are converted to porosity values and plotted on the left and the right, respectively, where they are compared to Neutron–Neutron porosity logging data.

and the simultaneous dense FWI in Fig. 5d. Note that all figures are plotted using true amplitude such that also amplitude differences can be observed.

The difference between the measured electric field and synthetically calculated electric field based on the ray-based tomography results is obvious (compare Fig. 5a and b). Data modeled using the ray-based

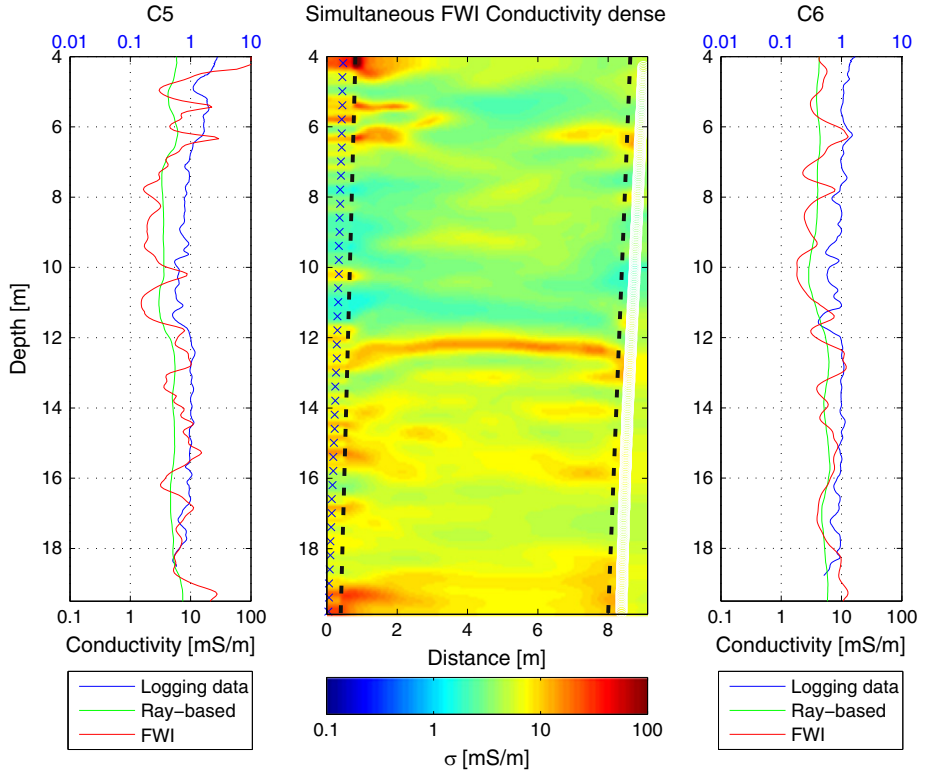

Fig. 7. Simultaneous dense conductivity FWI results at the last iteration number. Conductivity values indicated by the dashed white lines close to the C5 and C6 boreholes are plotted on the left and the right, respectively, and compared to capacitive conductivity logging data. Note the logarithmic conductivity scale for FWI result and the different scaling of the lower and upper horizontal axes for the logging data and FWI results.

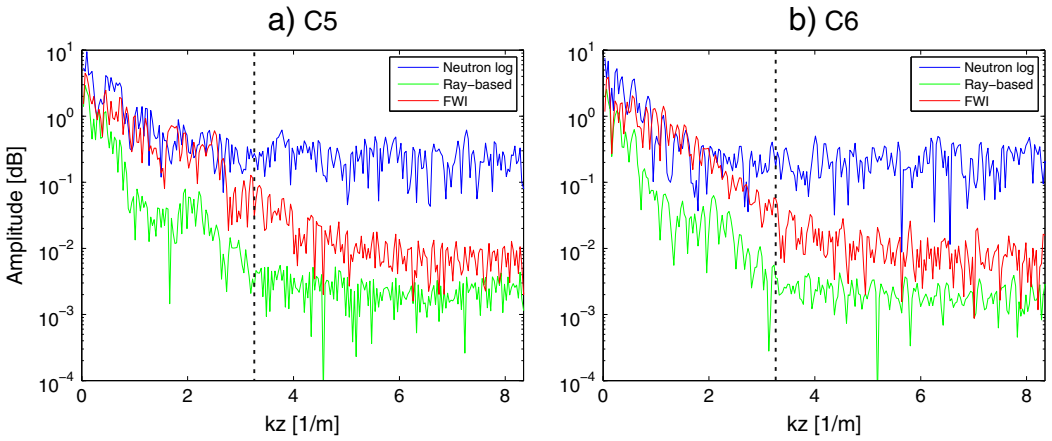

Fig. 8. Comparison of spatial frequency spectrums of a) C5 and b) C6 Neutron–Neutron logging data, ray-based tomography and FWI results in wavenumber frequency. A low-pass filter used to filter out the high frequency information is indicated by the dash lines.

inversion results return a poor match with the measured data and does not fit the observed data in detail, due to the use of the picked first arrivals only. This is the reason why only low-resolution images can be obtained with ray-based approaches.

Fig. 5c shows the synthetically calculated electric field based on the scalar FWI inversion results shown in Fig. 3c, d. It's evident that the scalar FWI version results fit better the observed data for transmitters T14–T38. However, still not all details in amplitude and phase of the measured electric field are visible in the synthetic data. Especially for transmitter T6 the modeled data does not resemble the measured data, which indicates that the scalar FWI version is not providing reliable results at small depth. The difference between the measured and modeled data is probably also generating the remaining gradients shown in Fig. 4c and d and probably is related with the presence of the artificial dipping feature that is interpreted as a numerical artifact.

Fig. 5d shows the synthetically calculated electric field based on the simultaneous dense FWI shown in Fig. 3i, j. Compared to the other modeling results, these data have a significantly better detailed fit with the measured data, not only in shape but especially also in amplitude. Since the measured data is fitting so well with the measured data it is clear that the obtained permittivity and conductivity models for the simultaneous FWI with dense acquisition setup realistically describe the medium properties present between the two boreholes.

5. Comparison to borehole logging data

To validate our inversion results in more detail, Neutron–Neutron porosity log data measured in the two boreholes C5 and C6 (Barrash and Clemo, 2002) are compared with the ray-based tomography and simultaneous dense FWI results obtained 30 cm away from the boreholes as indicated by the dashed white lines in Fig. 6. Note that the borehole logging data returns a high vertical resolution and a very low horizontal resolution, i.e. at only one horizontal position, whereas the tomography data returns a comparable horizontal and vertical intermediate resolution.

Earlier analysis of the correspondence between the scalar full-waveform inversion permittivity results and the Neutron–Neutron porosity log data ranged from poor to very good (Ernst et al., 2007a). Here, the obtained permittivities for the ray-based and simultaneous FWI are converted to porosity using the petrophysical model and parameters of Clement and Barrash (2006) and plotted in green and red lines, respectively on the left and the right in Fig. 6 for C5 and C6, respectively. The Neutron–Neutron counts return a proxy for water content and are transformed into porosity using the approach and parameters of Barrash and Clemo (2002) and Tronicke et al. (2004) and shown on the left and the right in Fig. 6 for boreholes C5 and C6, respectively.

A comparison of the ray-based porosity with the Neutron–Neutron porosity shows a clear difference in spatial resolution which is roughly

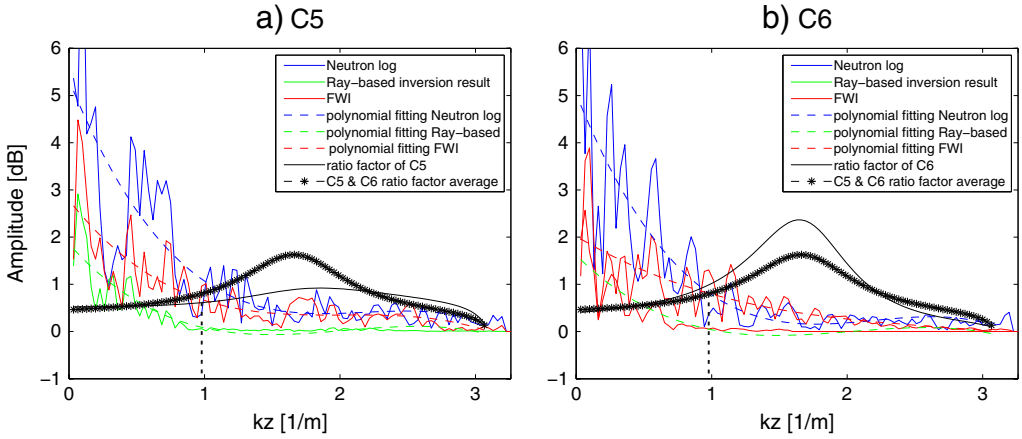

Fig. 9. Low wavenumber spectra for logging (blue), ray-based (green) and FWI (red) data, where pertaining polynomial fits are indicated by the dashed lines. The solid black line represents the wavenumber filter that weights the C5 and C6 logging data such that a similar spatial bandwidth is obtained as the FWI data. The asterisk lines represent the mean ratio factor of C5 and C6 that shows very similar amplitudes for low wavenumber values where most energy is present (black dashed lines).

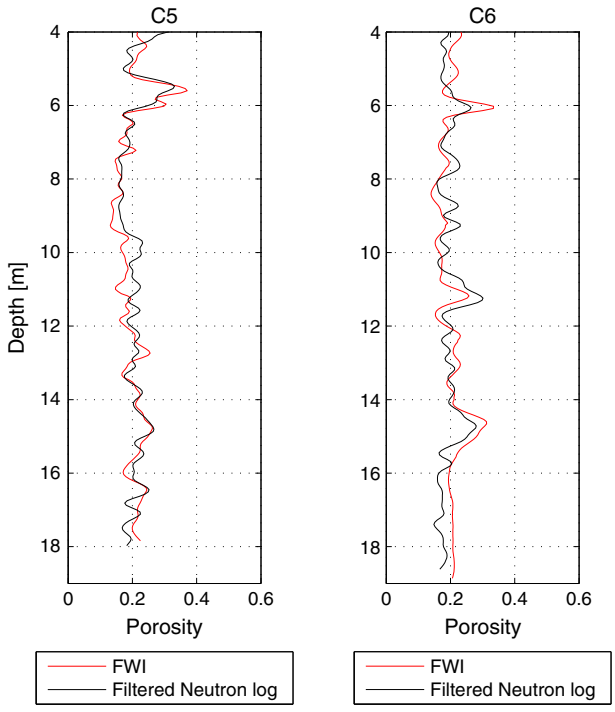

Fig. 10. The comparisons of filtered Neutron–Neutron log data using the filter we introduced in Section 5 and the converted permittivity simultaneous dense FWI results of boreholes C5 and C6.

one order of magnitude (Tronicke et al., 2004). The full-waveform inversion results show a significantly improved resolution and in general the absolute and relative porosity changes show a good correspondence. Especially, a good correspondence is obtained for high porosity values at ~5.7 m in borehole C5 and at ~6.0, and ~14.8 m in borehole C6. The relative changes between ~11 and ~17 m in C5 show a striking similarity. However, there is a static shift visible between ~9.5 and ~12 m in borehole C5 and below ~16 m in borehole C6.

Differences in resolutions can also be observed in Fig. 7 when comparing the capacitive conductivity log (Mwenifumbo et al., 2009) measured in boreholes C5 and C6 (blue line) with the conductivities of ray-based tomography and simultaneous FWI conductivity obtained close to boreholes C5 and C6 (green and red lines, respectively). Note the different scaling of the lower and upper horizontal axes for the logging data and the ray-based and logging data, which show an amplitude difference of one order of magnitude. This difference is partly due to the different frequencies used by the logging tool (1 MHz) and the GPR system (250 MHz), and difficult calibration of the logging tool (Tronicke et al., 2004).

5.1. Resolution analysis for an improved borehole and tomography comparison

Due to the different resolution obtained from the FWI results and borehole logging data, a direct comparison as shown in Figs. 6 and 7 can be difficult. To investigate the spatial information content of the logging data, ray-based and FWI results in Fig. 6 in more detail, Fig. 8a and b shows the absolute amplitudes of the spatial wavenumber content for boreholes C5 and C6, respectively, obtained by a fast Fourier transformation (FFT). Low, intermediate and high resolution information present in the ray-based (green), FWI (red) and logging (blue) data is characterized by a small bandwidth and low spatial frequencies, an intermediate bandwidth that includes also higher spatial frequencies, and a broad bandwidth that includes the highest spatial frequencies, respectively. Since the main information content in the Neutron–Neutron porosity log data is present for spatial wavenumbers smaller than $k_z = 3.2\ m^{-1}$ (see the dashed line in Fig. 8a, b), we will investigate the information content in the following only for vertical wavenumbers between $0 < k_z < 3.2\ m^{-1}$ and neglect higher spatial frequency information. Due to the FFT calculation and the interference of the real and imaginary parts of the events in the data the spectra shown in Fig. 9 contain highly fluctuating amplitudes. Polynomial curves are fitted through the logging, ray-based and FWI data and plotted as dashed lines and a comparison of the curves shown in Fig. 9a and b shows that the polynomial curves are very similar for C5 and C6, respectively.

To enable a better comparison between the logging and the FWI data shown in Fig. 9a, b, a wavenumber filter is calculated (black line) that weights the C5 and C6 logging wavenumber data such that a similar spatial bandwidth is obtained as the FWI data. Note the filter only corrects for wavenumber amplitudes and that the phases remain the same. To compare the C5 and C6 wavenumber filters the average is calculated and plotted as a dashed black line. Comparing the dashed and solid black lines in Fig. 9a and b shows that the filters are very similar for low spatial frequencies and deviate above $k_z > 1\ m^{-1}$. Due to the main energy (about 80%) being present below $k_z < 1\ m^{-1}$, these results indicate that the obtained wavenumber filter can be used to enable an improved comparison between FWI and logging data.

Fig. 10 shows that the FWI results are clearly fitting better the filtered Neutron–Neutron porosity data than the unfiltered Neutron–Neutron porosity data shown in Fig. 6. This is also indicated by the root mean square (RMS) values between the FWIs, and the original Neutron–Neutron porosity logs of C5 and C6 (see Fig. 6) are 0.0645 and 0.0629, respectively; whereas, the RMS values between the C5

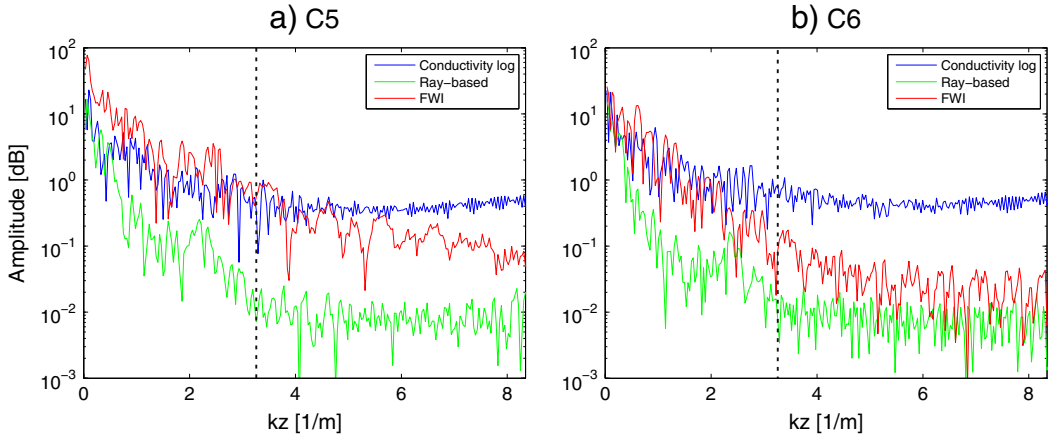

Fig. 11. The frequency spectrum comparisons of capacitive conductivity log data, ray-based tomography and FWI results in wavenumber frequency domain for C5 (a) and C6 (b). A low-pass filter used to filter out the high frequency information (indicated by dash lines) of capacitive conductivity log data.

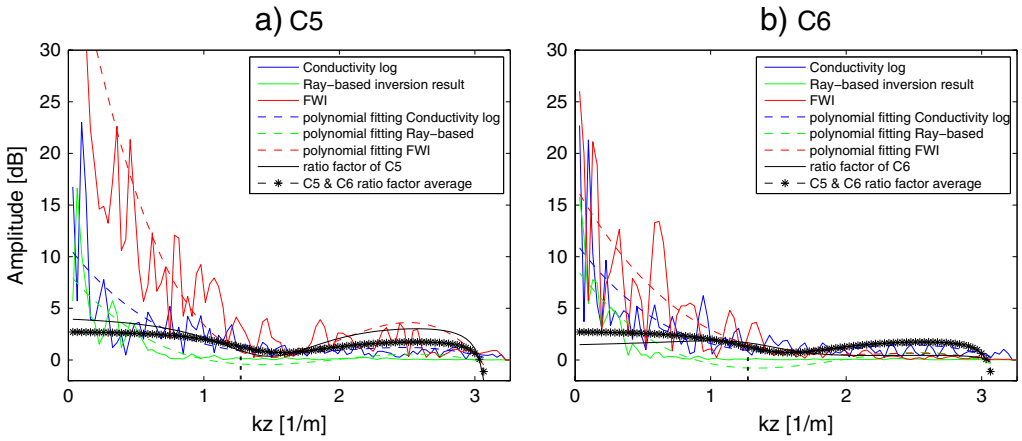

Fig. 12. Filter in wavenumber frequency domain for C5 (a) and C6 (b) capacitive conductivity log data. Polynomial fittings are used to make the filter more pervasive (indicated by the blue, green and red dash lines), the solid black line represents the ratio factors of C5 and C6, respectively. The asterisk line represents the mean ratio factor of C5 and C6.

and C6 FWIs and the filtered Neutron–Neutron porosity logs shown in Fig. 10 are 0.0345 and 0.0421, respectively.

The spatial frequency content is also investigated for the capacitive conductivity log data. Fig. 11a, b shows the spatial frequency spectrum of the logging data, ray-based and FWI results. Again the resolution information for the ray-based (green), FWI (red), and logging (blue) data is characterized by a small bandwidth of low spatial frequencies, an intermediate bandwidth that includes also higher spatial frequencies and a broad bandwidth that includes the highest spatial frequencies, respectively. The difference in spatial information content for the FWI and logging data is less consistent for low wavenumber values. Neglecting all spatial information for $k_z > 3.2\ m^{-1}$ and analyzing the data for wavenumbers $k_z < 3.2\ m^{-1}$ (see the dashed line in Fig. 11a, b) show that the spatial information content differs when comparing the C5 and C6 data. Also the obtained wavenumber filters are less similar for C5 and C6 compared to the filters obtained for the porosity data (Fig. 12). The filtered capacitive conductivity logging data and the FWI results look more similar in Fig. 13a, b for C5 and C6, respectively, compared to the unfiltered data in Fig. 7. A more detailed analysis of these results will be feasible when 1) improved calibration of the logging tool is possible, 2) quantitative FWI conductivity estimation can be performed, and 3) a better understanding is present for the one order of magnitude amplitude difference.

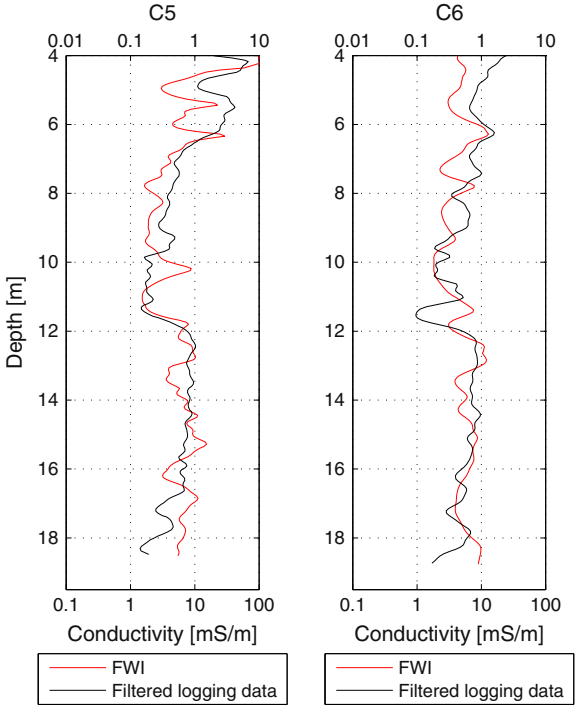

Fig. 13. The comparisons of filtered capacitive conductivity log data using the filter we introduced in Section 5 and simultaneous dense FWI results for C5 and C6. Note the logarithmic conductivity scale for FWI result and the different scaling of the lower and upper horizontal axes for the logging data and FWI results.

6. Conclusions

The BHRS data have been inverted with several versions of the FWI including a new version where all receiver positions (311 instead of 77) are used. To enable a comparison of the results, a normalized cost function and gradient are introduced that are not depending on the survey layout of the crosshole GPR measurements. Almost every improvement of the FWI resulted in a better fit of the synthetic data with the experimental data and shows the importance of including the vector character and using a simultaneous permittivity and conductivity update approach. Analyzing the remaining gradients at the final iteration shows that relatively large amplitude gradients remain at locations where numerical artifacts are present. This indicates that less reliable inversion results are obtained in regions with relatively high remaining gradient amplitudes. Using four times as many receivers resulted in similar inversion results as using the initial number of receivers.

A comparison of the FWI results with borehole logging data shows that higher spatial resolution is present in the logging data. Removing high spatial frequency information from the logging data and applying a wavenumber filter to compensate for the different spatial amplitudes result in an improved similarity between the FWI porosity results and the Neutron–Neutron porosity logging data. Designing a similar filter for the FWI conductivity results and comparison with capacitive conductivity logging data shows only a slight improvement.

The obtained results show the potential of FWI as an advanced method that is confirmed by Neutron–Neutron measurements that can provide high resolution subsurface images to improve hydrological models.

Acknowledgments

The first author thanks to the China Scholarship Council (CSC) for financial support. We thank the Jülich Supercomputing Center (JSC) for providing access to the JUROPA high performance cluster. We also thank Jonathan Mwenifumbo for allowing us to use the capacitive conductivity data from C6.

References

Barrash, W., Clemo, T., 2002. Hierarchical geostatistics and multifacies systems: Boise Hydrogeophysical Research Site, Boise, Idaho. Water Resour. Res. 38.

Barrash, W., Reboulet, E., 2004. Significance of porosity for stratigraphy and textural composition in subsurface, coarse fluvial deposits: Boise Hydrogeophysical Research Site. Geol. Soc. Am. Bull. 116, 1059–1073.

Barrash, W., Clemo, T., Knoll, M., 1999. Boise Hydrogeophysical Research Site (BHRS): objectives, design, initial geostatistical results, paper presented at Symposium on the Application of Geophysics to Engineering and Environmental Problems. Environ. and Eng. Geophys. Soc., Oakland, Calif.

Belina, F., Irving, J., Ernst, J., Holliger, K., 2012a. Analysis of an iterative deconvolution approach for estimating the source wavelet during waveform inversion of crosshole georadar data. J. Appl. Geophys. 78, 20–30.

Belina, F., Irving, J., Ernst, J., Holliger, K., 2012b. Evaluation of the reconstruction limits of a frequency-independent crosshole georadar waveform inversion scheme in the presence of dispersion. J. Appl. Geophys. 78, 9–19.

Binley, A., Winship, P., Middleton, R., Pokar, M., West, J., 2001. High-resolution characterization of vadose zone dynamics using cross-borehole radar. Water Resour. Res. 37, 2639–2652.

Binley, A., Cassiani, G., Middleton, R., Winship, P., 2002. Vadose zone flow model parameterisation using cross-borehole radar and resistivity imaging. J. Hydrol. 267, 147–159.

Bradford, J.H., Clement, W.P., Barrash, W., 2009. Estimating porosity with ground-penetrating radar reflection tomography: a controlled 3-D experiment at the Boise Hydrogeophysical Research Site. Water Resour. Res. 45.

Clement, W.P., Barrash, W., 2006. Crosshole radar tomography in a fluvial aquifer near Boise, Idaho. J. Environ. Eng. Geophys. 11, 171–184.

Dafflon, B., Barrash, W., 2012. Three-dimensional stochastic estimation of porosity distribution: benefits of using ground-penetrating radar velocity tomograms in simulated-annealing-based or Bayesian sequential simulation approaches. Water Resour. Res. 48.

Dafflon, B., Irving, J., Barrash, W., 2011. Inversion of multiple intersecting high-resolution crosshole GPR profiles for hydrological characterization at the Boise Hydrogeophysical Research Site. J. Appl. Geophys. 73, 305–314.

Deiana, R., Cassiani, G., Kemna, A., Villa, A., Bruno, V., Bagliani, A., 2007. An experiment of non-invasive characterization of the vadose zone via water injection and cross-hole time-lapse geophysical monitoring. Near Surf. Geophys. 5, 183–194.

Ernst, J.R., Maurer, H., Green, A.G., Holliger, K., 2007a. Full-waveform inversion of crosshole radar data based on 2-D finite-difference time-domain solutions of Maxwell's equations. IEEE Trans. Geosci. Remote Sens. 45, 2807–2828.

Ernst, J.R., Green, A.G., Maurer, H., Holliger, K., 2007b. Application of a new 2D time-domain full-waveform inversion scheme to crosshole radar data. Geophysics 72, J53–J64.

Gloaguen, E., Chouteau, M., Marcotte, D., Chapuis, R., 2001. Estimation of hydraulic conductivity of an unconfined aquifer using cokriging of GPR and hydrostratigraphic data. J. Appl. Geophys. 47, 135–152.

Holliger, K., Musil, M., Maurer, H., 2001. Ray-based amplitude tomography for crosshole georadar data: a numerical assessment. J. Appl. Geophys. 47, 285–298 (8th International Conference on Group Penetrating Radar (GRP 2000), GOLD COAST, AUSTRALIA, MAY 23–26, 2000).

Hubbard, S.S., Rubin, Y., Majer, E., 1997. Ground-penetrating-radar-assisted saturation and permeability estimation in bimodal systems. Water Resour. Res. 33, 971–990.

Irving, J., Knight, R., 2005. Effect of antennas on velocity estimates obtained from crosshole GPR data. Geophysics 70, K39–K42.

Irving, J.D., Knoll, M.D., Knight, R.J., 2007. Improving crosshole radar velocity tomograms: a new approach to incorporating high-angle travel time data. Geophysics 72, J31–J41.

Klotzsche, A., van der Kruk, J., Meles, G.A., Doetsch, J., Maurer, H., Linde, N., 2010. Full-waveform inversion of cross-hole ground-penetrating radar data to characterize a gravel aquifer close to the Thur River, Switzerland. Near Surf. Geophys. 8, 635–649.

Klotzsche, A., van der Kruk, J., Meles, G., Vereecken, H., 2012. Crosshole GPR full-waveform inversion of waveguides acting as preferential flow paths within aquifer systems. Geophysics 77, H57–H62.

Linde, N., Binley, A., Tryggvason, A., Pedersen, L.B., Revil, A., 2006. Improved hydrogeophysical characterization using joint inversion of crosshole electrical resistance and ground penetrating radar traveltime data. Water Resour. Res. 42, W12404. http://dx.doi.org/10.1029/2006WR005131.

Looms, M.C., Jensen, K.H., Binley, A., Nielsen, L., 2008. Monitoring unsaturated flow and transport using cross-borehole geophysical methods. Vadose Zone 7, 227–237.

Maurer, H., Musil, M., 2004. Effects and removal of systematic errors in crosshole georadar attenuation tomography. J. Appl. Geophys. 55, 261–270.

Meles, G.A., Van der Kruk, J., Greenhalgh, S.A., Ernst, J.R., Maurer, H., Green, A.G., 2010. A new vector waveform inversion algorithm for simultaneous updating of conductivity and permittivity parameters from combination crosshole/borehole-to-surface GPR data. IEEE Trans. Geosci. Remote Sens. 48, 3391–3407.

Meles, G., Greenhalgh, S., van der Kruk, J., Green, A., Maurer, H., 2011. Taming the non-linearity problem in GPR full-waveform inversion for high contrast media. J. Appl. Geophys. 73, 174–186.

Mwenifumbo, C.J., Barrash, W., Knoll, M.D., 2009. Capacitive conductivity logging and electrical stratigraphy in a high-resistivity aquifer, Boise Hydrogeophysical Research Site. Geophysics 74, E125–E133.

Oberröhrmann, M., Klotzsche, A., Vereecken, H., van der Kruk, J., 2013. Optimization of acquisition setup for cross-hole GPR full-waveform inversion using checkerboard analysis. Near Surf. Geophys. 11, 197–209.

Pratt, R., 1990. Frequency-domain elastic wave modeling by finite-differences — a tool for crosshole seismic imaging. Geophysics 55, 626–632.

Pratt, R., 1999. Seismic waveform inversion in the frequency domain, part 1: theory and verification in a physical scale model. Geophysics 64, 888–901.

Slater, L., Zaidman, M.D., Binley, A.M., West, L.J., 1997. Electrical imaging of saline tracer migration for the investigation of unsaturated zone transport mechanisms. Hydrol. Earth Syst. Sci. 1, 291–302.

Tarantola, A., 1984. Inversion of seismic-reflection data in the acoustic approximation. Geophysics 49, 1259–1266.

Tarantola, A., 1986. A strategy for nonlinear elastic inversion of seismic-reflection data. Geophysics 51, 1893–1903.

Topp, G., Davis, J., Annan, A., 1980. Electromagnetic determination of soil–water content — measurements in coaxial transmission-lines. Water Resour. Res. 16, 574–582.

Tronicke, J., Dietrich, P., Wahlig, U., Appel, E., 2002. Integrating surface georadar and crosshole radar tomography: a validation experiment in braided stream deposits. Geophysics 67, 1516–1523.

Tronicke, J., Holliger, K., Barrash, W., Knoll, M., 2004. Multivariate analysis of cross-hole georadar velocity and attenuation tomograms for aquifer zonation. Water Resour. Res. 40.

Virieux, J., Operto, S., 2009. An overview of full-waveform inversion in exploration geophysics. Geophysics 74, WCC1–WCC26.

Williamson, P., Worthington, M., 1993. Resolution limits in ray tomography due to wave behavior — numerical experiments. Geophysics 58, 727–735.

Winship, P., Binley, A., Gomez, D., 2006. Flow and transport in the unsaturated Sherwood Sandstone: characterization using cross-borehole geophysical methods. In: Barker, R.D., Tellam, J.H. (Eds.), Fluid Flow and Solute Movement in Sandstones: The Onshore UK Permo-triassic Red Bed Sequence, Environm & Ind Geophys Grp; Hydrogeol Grp Geol Soc London. Geological Soc Publishing House, Unit 7, Brassmill Enterprise Ctr, Brassmill Lane, Bath Ba1 3jn, Avon, England, pp. 219–231 (Meeting of the Environmental-and-Industrial-Geophysics-Group/Hydrogeological-Group of the Geological-Society-of-London, London, ENGLAND, 2003).

Zhou, B., Greenhalgh, S., 2003. Crosshole seismic inversion with normalized full-waveform amplitude data. Geophysics 68, 1320–1330.